Inorganic Chemistry

Article

Cite This: Inorg. Chem. 2019, 58, 6028−6036

pubs.acs.org/IC

The Role of Crystal Growth Conditions on the Magnetic Properties of $Ln_2Fe_{4-x}Co_xSb_5$ (Ln = La and Ce)

Ashley Weiland,[†] Sheng Li,[‡] Katherine A. Benavides,[†] Joseph V. Burnett,[†] JoAnna Milam-Guerrero,[§] Abbey J. Neer,[†] Gregory T. McCandless,[†] Bing Lv,[‡] and Julia Y. Chan*[,†]

[†]Department of Chemistry & Biochemistry, [‡]Department of Physics, University of Texas at Dallas, Richardson, Texas 75080, United States

[§]Department of Chemistry, University of Southern California, Los Angeles, California 90089, United States

Supporting Information

Downloaded via UNIV OF TEXAS AT DALLAS on May 7, 2019 at 19:25:50 (UTC).
See https://pubs.acs.org/sharingguidelines for options on how to legitimately share published articles.

ABSTRACT: Single crystals of $Ln_2Fe_{4-x}Co_xSb_{5-y}Bi_y$ (Ln = La, Ce; $0 \leq x < 0.5$; $0 \leq y \leq 0.2$) were grown using Bi flux and self-flux methods. The compounds adopt the $La_2Fe_4Sb_5$ structure type with tetragonal space group *I*4/*mmm*. The $La_2Fe_4Sb_5$ structure type is comprised of rare earth atoms capping square Sb nets in a square antiprismatic fashion and two transition-metal networks forming a PbO-type layer with Sb and transition-metal isosceles triangles. Substituting Co into the transition-metal sublattice results in a decrease in the transition temperature and reduced frustration, indicative of a transition from localized to itinerant behavior. In this manuscript, we demonstrated that Bi can be used as an alternate flux to grow single crystals of antimonides. Even with the incorporation of Bi into the Sb square net, the magnetic properties are not significantly affected. In addition, we have shown that the incorporation of Co into the Fe triangular sublattice leads to an itinerant magnetic system.

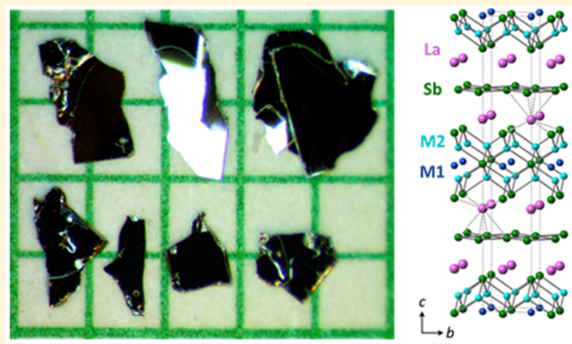

1. INTRODUCTION

Crystal structures containing antimony nets capped with rare earth ions, as in the layered $SmSb_2$ structure type,[1] have garnered significant interest because of their physical properties, including charge density waves,[2] large magnetoresistance,[3,4] and superconductivity.[5] The $SmSb_2$ structure type[1] is highly anisotropic, containing rectangular antimony nets capped by rare earth ions, and underpins the structures of ternary antimonides containing a transition-metal sublattice. $SmSb_2$ exhibits magnetoresistance of over 50000%,[3] and the isostructural $LaSb_2$ exhibits linear, nonsaturating magnetoresistance up to 45 T.[4] The incorporation of a transition-metal sublattice into the $SmSb_2$ structure type allows for the investigation of magnetism exhibited by compounds containing both localized *f*-electrons found in lanthanides and the traditionally itinerant *d*-electrons of transition metals. For example, $LnMSb_2$ (Ln = lanthanide; M = first row transition metal)[6] compounds of the $HfCuSi_2$ structure type[7] can be described as the $SmSb_2$ structure type with a tetrahedral transition-metal−antimony sublattice inserted.[8] Other examples of how the $SmSb_2$ structure type can be used as a building block to design new materials that can lead to exotic and complex electrical and magnetic properties have been recently reviewed.[8] Large magnetoresistance has been found in $LnNi_{1-x}Sb_2$ (Ln = Y, Dy, Ho; $x \sim 0.8$), where the magnetoresistance is above 100% at 3 K and 9 T.[9] Recent interest in the $HfCuSi_2$ structure type and structurally related compounds has been spurred by work on topological semimetals, such as $Sr_{1-y}Mn_{1-z}Sb_2$ (y, $z < 0.1$)[10] and $YbMnSb_2$,[11] where the Mn carries a magnetic moment in both compounds. The field of topological materials has been experiencing rapid recent growth[12,13] and materials containing Sb or Bi sheets have been found to host electronic band crossings that can result in topological phenomena.[14−22]

The $La_2Fe_4Sb_5$ structure type also consists of square Sb nets capped with rare earth and a sublattice of tetrahedrally coordinated transition metals[23] reminiscent of the PbO-type subunit found in the $HfCuSi_2$ structure type. In addition, the structure also possesses an additional Fe interspersed in the sublattice forming nearly equilateral triangles of Fe. As part of our study of layered and square net containing compounds, we have selected the $La_2Fe_4Sb_5$ structure type to investigate competing magnetic interactions.[24−26] In particular, we have focused our efforts on the incorporation of Co to study the impact on long-range magnetic ordering coupled with frustrated local environments. The magnetic susceptibility of $Ln_2Fe_4Sb_5$ (Ln = Ce−Nd, Sm) indicates that both the magnetic lanthanide sublattice and transition-metal sublattice carry magnetic moments and exhibit spin glass behavior.[27,28] $Pr_2Fe_{4-x}Co_xSb_5$ ($x \sim 1$) is antiferromagnetic below 25 K with an effective moment consistent with both a rare earth and

Received: February 4, 2019
Published: April 15, 2019

 © 2019 American Chemical Society

DOI: 10.1021/acs.inorgchem.9b00338
Inorg. Chem. 2019, 58, 6028−6036

Table 1. Crystallographic Parameters of $La_2Fe_4Sb_5$ and $La_2Fe_{4-x}Co_xSb_{4.8}Bi_{0.2}$ (x ~ 0 and 0.5)

	$La_2Fe_4Sb_5$	$La_2Fe_{4.14(6)}Sb_{4.76(4)}Bi_{0.22(3)}$ (x ~ 0)	$La_2M_{3.97(4)}Sb_{4.75(2)}Bi_{0.26(2)}$[a] (x ~ 0.5)
a (Å)	4.341(1)	4.348(3)	4.3395(16)
c (Å)	26.271(6)	26.175(18)	26.190(12)
V (Å^3)	495.0(3)	494.9(7)	493.2(4)
Z	2	2	2
T (K)	298	300	300
θ range (deg)	3.1−30.5	3.1−30.6	3.1−30.6
μ (mm^{-1})	27.52	30.90	32.05
measured reflections	1397	1660	2647
independent reflections	279	278	278
R_{int}	0.024	0.041	0.052
$\Delta\rho_{max}$ (e/Å^3)	3.11	2.31	2.69
$\Delta\rho_{min}$ (e/Å^3)	−2.52	−2.51	−3.70
extinction coefficient	0.00109(10)	0.0009(3)	0.0092(7)
data/restraints/parameters	279/0/22	278/0/23	278/0/22
R_1 ($F^2 > 2\sigma(F^2)$)	0.019	0.038	0.029
wR_2 (F^2)	0.035	0.094	0.072

[a]M = Fe, Co.

transition metal carrying a moment. A higher Co concentration (x ~ 2) results in antiferromagnetic ordering at 45 K and a second magnetic transition emerges at ~80 K. The deviation from Curie−Weiss behavior and emergence of a second magnetic transition is possibly due to the competition of localized and itinerant behavior.[28] To elucidate the role of transition-metal doping in the $La_2Fe_4Sb_5$ structure type, we focused on the synthesis and characterization of Co-incorporated La (nonmagnetic) and Ce (f^1) analogues. Herein, the single crystal synthesis using self-flux and Bi flux and the characterization of $Ln_2Fe_{4-x}Co_xSb_{5-y}Bi_y$ (Ln = La, Ce; $0 \leq x \leq 0.5$; $0 \leq y \leq 0.2$) is described and compared. We discuss the interplay of the transition-metal and lanthanide magnetic sublattices as a function of Co incorporation and present the magnetic susceptibility and electrical properties.

2. EXPERIMENTAL SECTION

2.1. Synthesis. The use of a Bi flux has led to the successful synthesis of compounds adopting the $La_2Fe_4Sb_5$ structure type.[27,28] Single crystals of $La_2Fe_{4-x}Co_xSb_{4.8}Bi_{0.2}$ (x ~ 0 and 0.5) and $Ce_2Fe_{4-x}Co_xSb_{4.8}Bi_{0.2}$ (x ~ 0.5) have been grown with stoichiometric mixtures of the elements and 10 mol of excess Bi as a flux in an alumina crucible that was capped with quartz wool and topped with an alumina catch crucible.[29] The reactions were sealed in fused silica tubing under ~1/3 atm Ar and placed in a furnace where they were then heated according to a temperature profile adapted from the synthesis of $Pr_2Fe_{4-x}Co_xSb_5$ ($x < 2.4$).[28] The reaction vessels were heated to 1150 °C at a rate of 100 °C/h, held for 72 h, cooled to 875 °C at a rate of 5 °C/h, removed from the furnace, and centrifuged to remove the excess Bi. Single crystals measuring up to ~0.5 mm were obtained using this method.

Thermogravimetric analysis coupled with differential scanning calorimetry (provided in the Supporting Information) of polycrystalline as-grown sample indicated a transition near 975 °C. Therefore, a second temperature profile with a slower cooling step was implemented in an effort to increase the size of the single crystals obtained from each reaction. The reaction vessels were heated to 1150 °C at a rate of 200 °C/h and dwelled for 24 h. The samples were cooled to 1000 °C at a rate of 10 °C/h and were slowly cooled at a rate of 2 °C/h to 900 °C. The reactions were then cooled to 875 °C at a rate of 5 °C/h, removed from the furnace, and centrifuged. Single crystals measuring up to ~1.5 mm were obtained using this synthetic protocol.

Single crystals of $La_2Fe_4Sb_5$ and $Ce_2Fe_4Sb_5$ were grown with a self-flux using a ratio of 1Ln/2Fe/3Sb (Ln = La, Ce). The elements were placed in an alumina crucible and sealed in an iron tube, which was then sealed in an evacuated quartz tube to avoid oxidation. The reaction was heated to 650 °C, dwelled for 10 h, heated to 1170 °C, dwelled for 48 h, and then cooled to 900 °C at a rate of 3 °C/h.

2.2. Structure Determination. Phase identification, sample homogeneity, and crystal structures were determined by single crystal X-ray diffraction. Single crystals were cut to appropriate sizes and mounted on glass fibers with two-part epoxy. The fibers were mounted on a Bruker D8 Quest Kappa single-crystal X-ray diffractometer equipped with a Mo Kα IμS microfocus source (λ = 0.71073 Å) operating at 50 kV and 1 mA with a HELIOS optic monochromator and a CMOS detector. The collected data were corrected for absorption using the Bruker program SADABS (multiscan method).[30] Starting crystallographic models were obtained using the intrinsic phasing method in SHELXT,[31] and atomic sites were refined anisotropically using SHELXL2014.[32] According to data obtained from single crystal refinement, the compounds grown in the Bi flux contain a Bi incorporation of ~0.2. The compounds are referred to as $Ln_2Fe_{4-x}Co_xSb_{4.8}Bi_{0.2}$ (Ln = La, Ce; $0 \leq x < 0.5$). Crystallographic parameters and refinement details for $La_2Fe_4Sb_5$ and $La_2Fe_{4-x}Co_xSb_{4.8}Bi_{0.2}$ (x ~ 0 and 0.5) are provided in Table 1 and for $Ce_2Fe_4Sb_5$ and $Ce_2Fe_{4-x}Co_xSb_{4.8}Bi_{0.2}$ (x ~ 0.5) in Table 2. Atomic

Table 2. Crystallographic Parameters of $Ce_2Fe_4Sb_5$ and $Ce_2Fe_{4-x}Co_xSb_{4.8}Bi_{0.2}$ (x ~ 0.5)

	$Ce_2Fe_4Sb_5$	$Ce_2M_{4.11(3)}Sb_{4.78(2)}Bi_{0.23(2)}$[a]
a (Å)	4.3087(7)	4.3198(16)
c (Å)	26.001(5)	25.851(9)
V (Å^3)	482.71(19)	482.4(4)
Z	2	2
T (K)	298	299
θ range (deg)	3.1−30.5	3.2−30.6
μ (mm^{-1})	28.70	32.66
measured reflections	1641	2778
independent reflections	272	273
R_{int}	0.037	0.030
$\Delta\rho_{max}$ (e/Å^3)	1.65	2.90
$\Delta\rho_{min}$ (e/Å^3)	−2.50	−2.23
extinction coefficient	0.0050(5)	0.0050(3)
data/restraints/parameters	272/0/21	273/0/22
R_1 ($F^2 > 2\sigma(F^2)$)	0.028	0.021
wR_2 (F^2)	0.064	0.045

[a]M = Fe, Co.

DOI: 10.1021/acs.inorgchem.9b00338
Inorg. Chem. 2019, 58, 6028−6036

Table 3. Atomic Positions of $Ln_2Fe_4Sb_5$ and $Ln_2Fe_{4-x}Co_xSb_{4.8}Bi_{0.2}$ (Ln = La, Ce; $x \sim 0$ and 0.5)

atom	Wyckoff site	point symm.	x	y	z	occ.	U_{eq} [a] (Å^2)
$La_2Fe_4Sb_5$							
La1	4*e*	4*mm*	0	0	0.34753(2)	1	0.00941(15)
Fe1	2*a*	4/*mmm*	0	0	0	1	0.0139(4)
Fe2	8*g*	2*mm*	0	1/2	0.45037(6)	0.764(6)	0.0279(6)
Sb1	4*d*	$\bar{4}m2$	0	1/2	1/4	1	0.01000(16)
Sb2	4*e*	4*mm*	0	0	0.10773(3)	1	0.00982(17)
Sb3	8*j*	*m*2*m*	0	0.0749(6)	1/2	0.252(2)	0.0433(13)
$La_2Fe_{4.14(6)}Sb_{4.76(4)}Bi_{0.22(3)}$							
La1	4*e*	4*mm*	0	0	0.34797(5)	1	0.0069(4)
Fe1	2*a*	4/*mmm*	0	0	0	1	0.0113(11)
Fe2	8*g*	2*mm*	0	1/2	0.45043(13)	0.788(15)	0.0279(15)
Sb1	4*d*	$\bar{4}m2$	0	1/2	1/4	0.889(14)	0.0081(5)
Bi1	4*d*	$\bar{4}m2$	0	1/2	1/4	0.111(14)	0.0081(5)
Sb2	4*e*	4*mm*	0	0	0.10772(6)	1	0.0071(4)
Sb3	8*j*	*m*2*m*	0	0.0845(12)	1/2	0.247(5)	0.029(2)
$La_2M_{3.97(4)}Sb_{4.75(2)}Bi_{0.26(2)}$ ($x \sim 0.5$)							
La1	4*e*	4*mm*	0	0	0.34827(3)	1	0.0035(3)
M1	2*a*	4/*mmm*	0	0	0	1	0.0065(6)
M2	8*g*	2*mm*	0	1/2	0.44980(8)	0.742(11)	0.0175(8)
Sb1	4*d*	$\bar{4}m2$	0	1/2	1/4	0.870(10)	0.0043(3)
Bi1	4*d*	$\bar{4}m2$	0	1/2	1/4	0.130(10)	0.0043(3)
Sb2	4*e*	4*mm*	0	0	0.10770(4)	1	0.0034(3)
Sb3	4*e*	4*mm*	0	0	0.4927(4)	0.505(7)	0.052(2)
$Ce_2Fe_4Sb_5$							
Ce1	4*e*	4*mm*	0	0	0.34718(3)	1	0.0091(3)
Fe1	2*a*	4/*mmm*	0	0	0	1	0.0136(6)
Fe2	8*g*	2*mm*	0	1/2	0.44924(8)	0.750(11)	0.0315(11)
Sb1	4*d*	$\bar{4}m2$	0	1/2	1/4	1	0.0094(3)
Sb2	4*e*	4*mm*	0	0	0.10977(4)	1	0.0093(3)
Sb3	4*e*	4*mm*	0	0	0.48522(12)	0.497(7)	0.0379(10)
$Ce_2M_{4.11(3)}Sb_{4.78(2)}Bi_{0.23(2)}$ ($x \sim 0.5$)							
Ce1	4*e*	4*mm*	0	0	0.34810(2)	1	0.0058(2)
M1	2*a*	4/*mmm*	0	0	0	1	0.0116(5)
M2	8*g*	2*mm*	0	1/2	0.44884(6)	0.778(8)	0.0198(7)
Sb1	4*d*	$\bar{4}m2$	0	1/2	1/4	0.886(8)	0.0067(3)
Bi1	4*d*	$\bar{4}m2$	0	1/2	1/4	0.114(8)	0.0067(3)
Sb2	4*e*	4*mm*	0	0	0.10947(3)	1	0.0059(2)
Sb3	4*e*	4*mm*	0	0	0.4932(5)	0.503(6)	0.054(3)

[a] U_{eq} is defined as one-third of the trace of the orthogonalized U_{ij} tensor. M1 and M2 represent transition metals.

coordinates, anisotropic displacement parameters, and partial occupancies for all analogues are included in Table 3. Select interatomic distances and angles are provided in Table 4.

2.3. Physical Properties. Magnetic measurements of single crystals of $Ln_2Fe_{4-x}Co_xSb_{5-y}Bi_y$ (Ln = La, Ce; $0 \le x \le 0.5$; $0 \le y \le 0.2$) were performed using a Quantum Design magnetic property measurement system (MPMS). Direct current magnetic susceptibility data were collected under zero-field-cooled (ZFC) and field-cooled (FC) conditions under an applied field of 0.1 T from 3 to 300 K. Field-dependent magnetization data were collected at 5 K with applied magnetic fields up to 3 T for the La analogues and at 2 K with fields up to 14 T for the Ce analogues. Temperature-dependent electrical resistivity was performed on $La_2Fe_{4-x}Co_xSb_{4.8}Bi_{0.2}$ ($x \sim 0.5$) and $Ce_2Fe_{4-x}Co_xSb_{4.8}Bi_{0.2}$ ($x \sim 0.5$) single crystals using a Quantum Design physical property measurement system (PPMS), using the four-probe method with Au wire adhered with Ag epoxy.

3. RESULTS AND DISCUSSION

3.1. Structure. $Ln_2Fe_{4-x}Co_xSb_{5-y}Bi_y$ (Ln = La, Ce; $0 \le x \le 0.5$; $0 \le y \le 0.2$) are isostructural to $La_2Fe_4Sb_5$ with the tetragonal space group *I*4/*mmm*, Figure 1.[23] The structure consists of Ln in a square antiprismatic environment with Sb. The transition-metal−antimony sublattice lies between Sb1 square net layers and is comprised of two metal sites (M1 and M2) occupied by Fe and Co and two antimony sites (Sb2 and Sb3). The M2 site is tetrahedrally coordinated to the Sb, forming an arrangement that can be considered two PbO-like slabs that are connected in the *c* direction to form a "cage-like"

DOI: 10.1021/acs.inorgchem.9b00338
Inorg. Chem. 2019, 58, 6028−6036

Table 4. Selected Interatomic Distances and Angles

	$La_2Fe_4Sb_5$	$La_2Fe_4Sb_{4.8}Bi_{0.2}$ ($x \sim 0$)	$La_2Fe_{4-x}Co_xSb_{4.8}Bi_{0.2}$ ($x \sim 0.5$)
Distance (Å)			
M1-M2 (×8)	2.5320(9)	2.532(2)	2.5369(13)
M2-M2 (×1)	2.608(3)	2.595(7)	2.629(4)
M2-Sb2 (×2)	2.6535(11)	2.654(2)	2.6413(15)
M2-Sb3 (×2)	2.260(2)	2.225(5)	2.443(5)
M2-Sb3′ (×2)	2.5528(10)	2.558(2)	2.641(6)
Angle (deg)			
M2-M1-M2	61.99(6)	61.66(14)	62.42(9)
M1-M2-M2	59.01(3)	59.17(7)	58.79(4)

	$Ce_2Fe_4Sb_5$	$Ce_2Fe_{4-x}Co_xSb_{4.8}Bi_{0.2}$ ($x \sim 0.5$)
Distance (Å)		
M1-M2 (×8)	2.5264(11)	2.5327(11)
M2-M2 (×1)	2.640(4)	2.645(3)
M2-Sb2 (×2)	2.6449(13)	2.6338(12)
M2-Sb3 (×2)	2.3487(14)	2.445(6)
M2-Sb3′ (×2)	2.629(7)	
Angle (deg)		
M2-M1-M2	62.98(8)	62.96(7)
M1-M2-M2	58.51(4)	58.52(3)

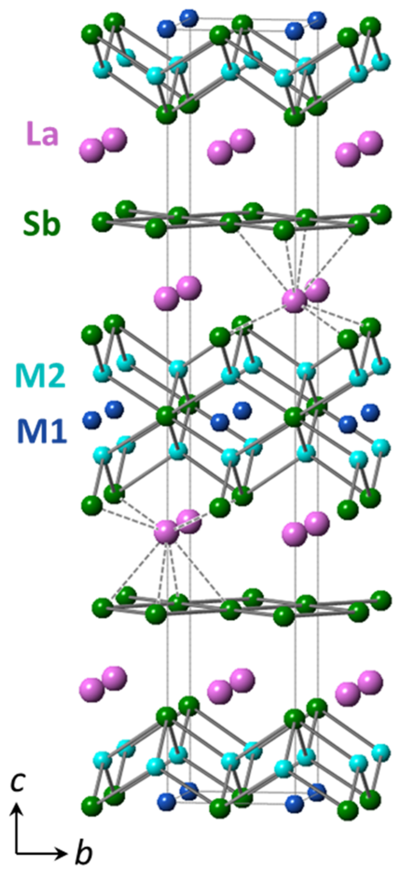

Figure 1. Crystal structure of $La_2Fe_4Sb_5$. La is shown in pink, M1 and M2 in blue, and Sb in green. The coordination environment of La is shown using dashed lines.

structure. The M1 site resides in the voids of the "cage" and is close enough to the M2 sites to be considered interacting (~2.5 Å), forming a triangular network with the M2 sites, where M2-M2 ~ 2.6 Å.

As shown in Table 4, the bond distances within the transition-metal sublattice remain relatively unchanged upon incorporation of Bi for $La_2Fe_{4-x}Co_xSb_{4.8}Bi_{0.2}$ compared to $La_2Fe_4Sb_5$. However, upon Co substitution, the M1-M2 and M2-M2 distances increase slightly. Similarly, the distances of the transition-metal sublattice of $Ce_2Fe_{4-x}Co_xSb_{4.8}Bi_{0.2}$ ($x \sim 0.5$) are comparable to $Ce_2Fe_4Sb_5$. In the $La_2Fe_4Sb_5$ structure type, the M2 site of the transition-metal−antimony sublattice is partially occupied and the Sb3 site is modeled as a split site due to a large atomic displacement parameter (ADP).[27] The M2 site occupancy of the La analogues decreases upon Co incorporation, which is counter to what was observed in the Ce and Pr analogues.

Single crystal structure determination and elemental analysis revealed Bi incorporation in the $Ln_2Fe_{4-x}Co_xSb_{4.8}Bi_{0.2}$ samples. Bonds between Bi and Co are exceptionally rare and are found in materials synthesized by applying high pressure. In the case of $CoBi_3$, 5 GPa of pressure and a temperature of 723 K were required to stabilize the binary phase, and the Co−Bi bond distances were reported to range from 2.700(7)−2.79(1) Å.[33,34] Similarly, the synthesis of $FeBi_2$ required a temperature of 1500 K and a pressure of 30 GPa, and the bond distance of Fe−Bi is reported to be ~2.719(2) Å.[35] The distances between the transition-metal and antimony sites in $La_2Fe_{4-x}Co_xSb_{4.8}Bi_{0.2}$ ($x \sim 0$ and 0.5) and $Ce_2Fe_{4-x}Co_xSb_{4.8}Bi_{0.2}$ ($x \sim 0.5$) range from 2.225(5)−2.654(2) Å, which are shorter than the distances reported in the $CoBi_3$ and $FeBi_2$ binaries. It was, therefore, demonstrated that Bi would substitute onto the Sb1 site of the antimony net rather than onto the Sb2 or Sb3 sites, which would necessitate the formation of a Fe−Bi or Co−Bi bond. Additionally, allowing the occupancy of the Sb1 site of the square Sb net to freely refine yields occupancy that is greater than 100% which indicates additional electron density not modeled. The crystallographic models presented here show atomic mixing of Bi and Sb on the Sb1 site where the occupancy is constrained to 100%. The observation of Bi substitution in the square nets was also reported in $CeNi_{1-x}Sb_{1+y}Bi_{1-y}$, where a maximum of 50% Bi incorporation into the square nets was coupled with subsequent Ni defects.[36] The $Ln_2Fe_{4-x}Co_xSb_{4.8}Bi_{0.2}$ were grown with a Ce/Bi ratio of 1:5, which possibly led to a lower concentration of Bi. Unlike for the reported $CeNi_{1-x}Sb_{1+y}Bi_{1-y}$, we do not see a reduction in the occupancy of the transition-metal site upon Bi incorporation.

3.2. Magnetic Properties. *$La_2Fe_4Sb_{4.8}Bi_{0.2}$ and $La_2Fe_{4-x}Co_xSb_{4.8}Bi_{0.2}$ ($x \sim 0.5$).* The temperature-dependent magnetic susceptibility of $La_2Fe_{4-x}Co_xSb_{4.8}Bi_{0.2}$ ($x \sim 0$ and 0.5) is shown in Figure 2. The magnetization as a function of applied field is provided in Figure 3. The magnetic susceptibility of $La_2Fe_4Sb_{4.8}Bi_{0.2}$ is similar to the susceptibility of $La_2Fe_4Sb_5$[27] as both samples exhibit a transition at ~32 K. The susceptibility data of $La_2Fe_4Sb_{4.8}Bi_{0.2}$ were fit in the range of 80−300 K using the modified Curie−Weiss law $\chi(T) = \chi_0 + C/(T - \theta_w)$, where χ_0 represents the temperature-independent contribution to the magnetic susceptibility, C is the Curie constant, and θ_w is the Weiss temperature. The values obtained from the modified Curie−Weiss fit are compared in Table 5. The Weiss temperature is highly dependent on the temperature range of the fit. However, the overall trend is that θ_w decreases as Co is incorporated into the lattice. The effective magnetic moment of $La_2Fe_4Sb_{4.8}Bi_{0.2}$ is 5.4 μ_B/mol-transition

DOI: 10.1021/acs.inorgchem.9b00338
Inorg. Chem. 2019, 58, 6028−6036

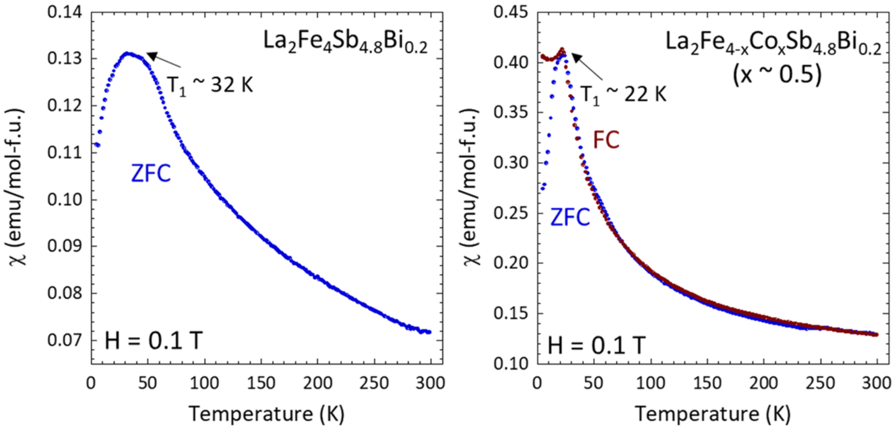

Figure 2. Temperature-dependent magnetic susceptibility of $La_2Fe_4Sb_{4.8}Bi_{0.2}$ and $La_2Fe_{4-x}Co_xSb_{4.8}Bi_{0.2}$ ($x \sim 0.5$). The field cooled data are shown in red, and the zero-field cooled data are shown in blue. Field cooled data for $La_2Fe_4Sb_{4.8}Bi_{0.2}$ can be found in the Supporting Information.

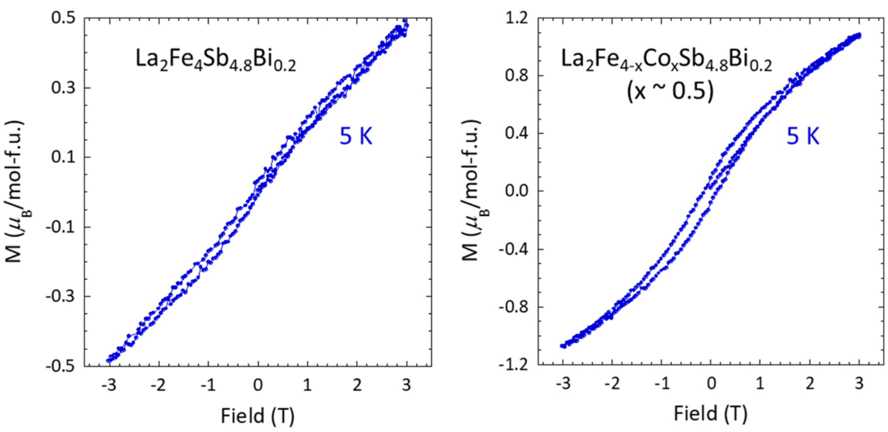

Figure 3. Field-dependent magnetization of $La_2Fe_4Sb_{4.8}Bi_{0.2}$ and $La_2Fe_{4-x}Co_xSb_{4.8}Bi_{0.2}$ ($x \sim 0.5$) collected at 5 K.

Table 5. Magnetic Properties of $La_2Fe_{4-x}Co_xSb_{4.8}Bi_{0.2}$ ($x \sim 0$ and 0.5)

compound	fit region	χ_0 (emu/mol-f.u.)	θ_w (K)	μ_{eff} (μ_B/mol-M)	T_1 (K)
$La_2Fe_4Sb_{4.8}Bi_{0.2}$	80−300 K	0.03487(2)	−123(1)	5.4	32
$La_2Fe_{4-x}Co_xSb_{4.8}Bi_{0.2}$ ($x \sim 0.5$)	100−300 K	0.0909(1)	−18.0(4)	4.9	22

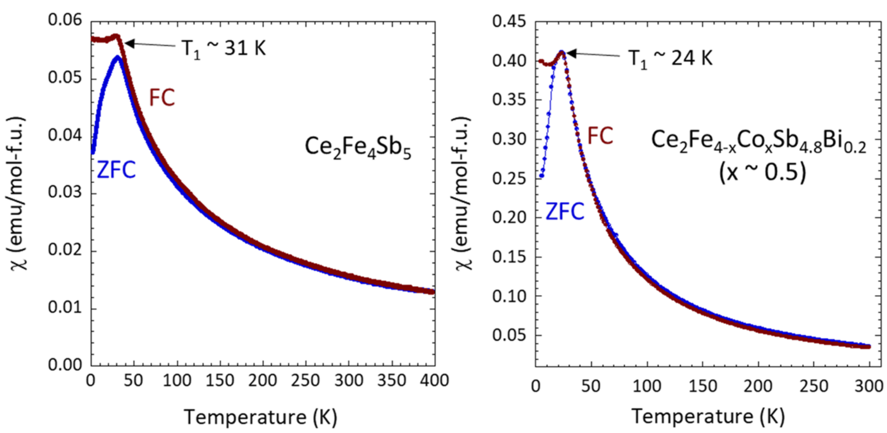

Figure 4. Temperature-dependent magnetic susceptibility of $Ce_2Fe_4Sb_5$ and $Ce_2Fe_{4-x}Co_xSb_{4.8}Bi_{0.2}$ ($x \sim 0.5$). The field cooled data are shown in red, and the zero-field cooled data are shown in blue.

metal. The magnetic moment is within the range of Fe^{2+} (4.9 μ_B) and Fe^{3+} (5.9 μ_B) oxidation state.

For $La_2Fe_{4-x}Co_xSb_{4.8}Bi_{0.2}$ ($x \sim 0.5$), the magnetic susceptibility exhibits a bifurcation between the ZFC and FC data, but the transition temperature decreases from ∼32 K to ∼22 K and the magnetization at T_1 (∼22 K) increases from ∼0.13 to ∼0.41 emu/mol relative to $La_2Fe_4Sb_{4.8}Bi_{0.2}$. The magnetic susceptibility data were fit in the range of 100−300 K

DOI: 10.1021/acs.inorgchem.9b00338
Inorg. Chem. 2019, 58, 6028−6036

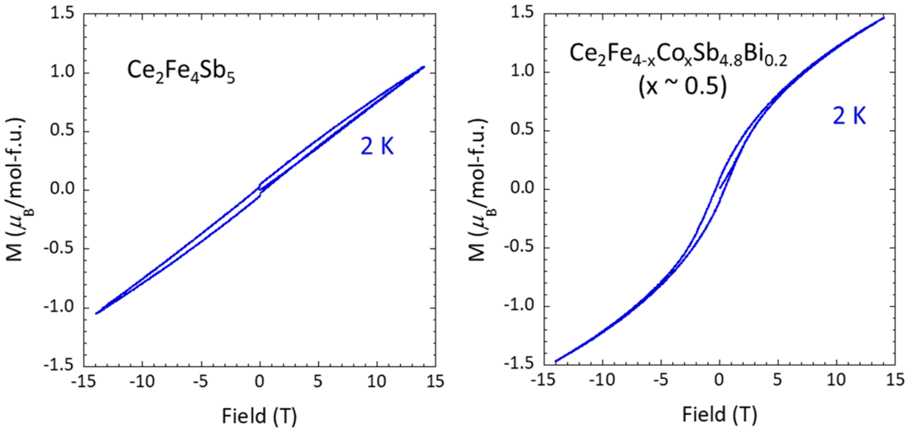

Figure 5. Field-dependent magnetization of $Ce_2Fe_4Sb_5$ and $Ce_2Fe_{4-x}Co_xSb_{4.8}Bi_{0.2}$ ($x \sim 0.5$) collected at 2 K.

Table 6. . Magnetic Properties of $Ce_2Fe_4Sb_5$ and $Ce_2Fe_{4-x}Co_xSb_{4.8}Bi_{0.2}$ ($x \sim 0.5$)

compound	fit region	χ_0 (emu/mol-f.u.)	θ (K)	μ_{eff} (μ_B/mol-M)	T_1 (K)
$Ce_2Fe_4Sb_5$	200−400 K	n/a	−118	3.17	31
$Ce_2Fe_{4-x}Co_xSb_{4.8}Bi_{0.2}$ ($x \sim 0.5$)	100−300 K	−0.0104(2)	−1.2	4.88	24

using a modified Curie−Weiss law, and the results are included in Table 5. The effective magnetic moment obtained from the fit of the magnetic data is 4.9 μ_B/mol-transition metal, in agreement with an Fe^{2+} system. The decrease in transition temperature is likely due to the increased M2-M2 distances within the transition-metal triangular sublattice. The Weiss temperature of −18.0(4) K is also significantly reduced relative to the −123(1) K of $La_2Fe_4Sb_{4.8}Bi_{0.2}$, suggesting that the system is less frustrated upon incorporating Co. The field-dependent magnetization shows that the magnetization of $La_2Fe_{4-x}Co_xSb_{4.8}Bi_{0.2}$ ($x \sim 0.5$) increases from ~0.48 μ_B/mol to ~1.08 μ_B/mol at 3 T. The hysteretic behavior of $La_2Fe_{4-x}Co_xSb_{4.8}Bi_{0.2}$ ($x \sim 0.5$) at 5 K also becomes more pronounced with increasing Co concentration with the remanent magnetization increasing from ~0.02 μ_B/mol to ~0.09 μ_B/mol.

The magnetization as a function of applied magnetic field is also similar for $La_2Fe_4Sb_{4.8}Bi_{0.2}$ and $La_2Fe_4Sb_5$.[27] Both compounds exhibit a small hysteresis, and the remanent magnetizations are comparable at ~0.02 μ_B/mol. The similarity in magnetic behavior is not unexpected, given that the interatomic distances of the transition-metal sublattice do not change drastically upon substituting Bi into the structure. These results indicate that the addition of Bi does not significantly impact the magnetic properties of compounds adopting the $La_2Fe_4Sb_5$ structure type.

$Ce_2Fe_4Sb_5$ and $Ce_2Fe_{4-x}Co_xSb_{4.8}Bi_{0.2}$ ($x \sim 0.5$). The temperature-dependent magnetic susceptibility of $Ce_2Fe_4Sb_5$ and $Ce_2Fe_{4-x}Co_xSb_{4.8}Bi_{0.2}$ ($x \sim 0.5$) is shown in Figure 4, and the magnetization as a function of applied magnetic field is shown in Figure 5. The susceptibility of $Ce_2Fe_4Sb_5$ was fit using the Curie−Weiss law, and that for $Ce_2Fe_{4-x}Co_xSb_{4.8}Bi_{0.2}$ ($x \sim 0.5$) was fit using a modified Curie−Weiss law; details are provided in Table 6. $Ce_2Fe_4Sb_5$ has an antiferromagnetic transition temperature of ~31 K with a total magnetic moment of 7.29 μ_B/mol-compound. When the calculated moment for Ce^{3+} is subtracted, 3.17 μ_B/mol-transition metal remains, indicating a possible itinerant magnetic sublattice. For $Ce_2Fe_{4-x}Co_xSb_{4.8}Bi_{0.2}$ ($x \sim 0.5$), the addition of Co results in the transition temperature decreasing from ~31 to ~24 K, similar to the trend observed for incorporating Co in the La analogues. The total effective moment obtained for the $x \sim 0.5$ analogue is 10.4 μ_B/mol-compound. When the calculated moment of Ce^{3+} is taken into account, the contribution from the transition-metal sublattice is 4.88 μ_B/mol-transition metal. The transition-metal moment is close to the moment obtained for $La_2Fe_{4-x}Co_xSb_{4.8}Bi_{0.2}$ ($x \sim 0.5$) and corresponds to a Fe^{2+} system (4.9 μ_B). The absolute value of the Weiss temperature decreases as Co is incorporated into the lattice, similar to what is seen in La analogues.

The field-dependent magnetization of $Ce_2Fe_{4-x}Co_xSb_{4.8}Bi_{0.2}$ ($x \sim 0.5$), as shown on the right in Figure 5, does not show significant change compared to self-flux grown $Ce_2Fe_4Sb_5$. The remanent magnetization of $Ce_2Fe_{4-x}Co_xSb_{4.8}Bi_{0.2}$ ($x \sim 0.5$) of ~0.19 μ_B/mol is comparable to the remanent magnetization of $Ce_2Fe_4Sb_5$, ~0.09 μ_B/mol. The magnetization of $Ce_2Fe_{4-x}Co_xSb_{4.8}Bi_{0.2}$ ($x \sim 0.5$) at 2 K and 15 T also increases from ~1 μ_B/mol observed in $Ce_2Fe_4Sb_5$ to ~1.4 μ_B/mol.

3.3. Electrical Resistivity. *$La_2Fe_4Sb_5$ and $La_2Fe_{4-x}Co_xSb_{4.8}Bi_{0.2}$ ($x \sim 0.5$).* The temperature-dependent electrical resistivities of $La_2Fe_4Sb_5$ and $La_2Fe_{4-x}Co_xSb_{4.8}Bi_{0.2}$ ($x \sim 0.5$) were normalized to ρ(300 K) and are shown in Figure 6. The parent compound exhibits metallic behavior with a resistivity on the order of ~195 $\mu\Omega\cdot$cm at room temperature.[27] At ~75 K the resistivity increases with decreasing temperature and continues to do so until ~30 K, when the resistivity starts to decrease again. $La_2Fe_{4-x}Co_xSb_{4.8}Bi_{0.2}$ ($x \sim 0.5$) exhibits resistivity on the order of ~75 $\mu\Omega\cdot$cm at room temperature, less than half the resistivity of $La_2Fe_4Sb_5$. The addition of Co suppresses the increased resistivity at low temperature ($T \sim 75$ K) observed in the parent compound that was described as "Kondo-like".[27]

$Ce_2Fe_4Sb_5$ and $Ce_2Fe_{4-x}Co_xSb_{4.8}Bi_{0.2}$ ($x \sim 0.5$). The temperature-dependent electrical resistivity of $Ce_2Fe_{4-x}Co_xSb_{4.8}Bi_{0.2}$ ($x \sim 0.5$) was normalized to ρ(300 K) and plotted with the parent compound,[27] as shown in Figure 7. The Ce analogues exhibit metallic character before reaching a transition temperature (T_K) where the resistivity increases with decreasing temperature. A second transition at ~30 K is marked by a decrease in resistivity with decreasing temper-

DOI: 10.1021/acs.inorgchem.9b00338
Inorg. Chem. 2019, 58, 6028−6036

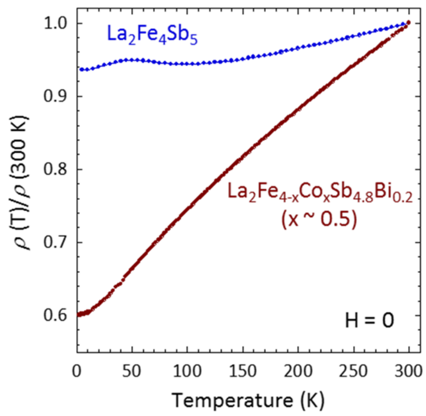

Figure 6. Normalized temperature-dependent resistivities of $La_2Fe_4Sb_5$ and $La_2Fe_{4-x}Co_xSb_{4.8}Bi_{0.2}$ (x ~ 0.5). The $La_2Fe_{4-x}Co_xSb_{4.8}Bi_{0.2}$ (x ~ 0.5) data are shown in red. The $La_2Fe_4Sb_5$ data, shown in blue, are replotted from ref 27.

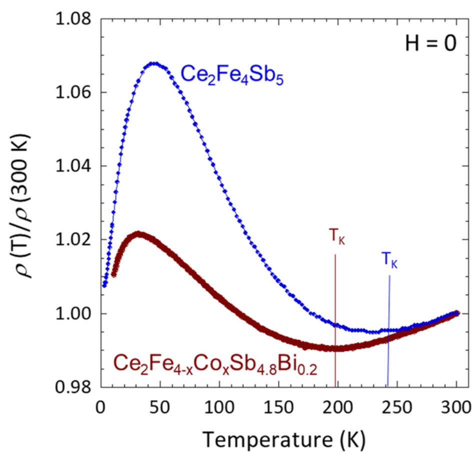

Figure 7. Normalized temperature-dependent resistivities of $Ce_2Fe_4Sb_5$ (x = 0) and $Ce_2Fe_{4-x}Co_xSb_{4.8}Bi_{0.2}$ (x ~ 0.5). The $Ce_2Fe_{4-x}Co_xSb_{4.8}Bi_{0.2}$ (x ~ 0.5) data are shown in red. The $Ce_2Fe_4Sb_5$, data, shown in blue, are replotted from ref 27.

ature. This behavior could be attributed to the Kondo effect where the increase in resistivity is due to electron scattering and the subsequent decrease is due to the development of coherence.[37] The Kondo effect is the screening of localized moments by the conduction electrons of a material at sufficiently low temperature[37,38] and is known to occur for dilute magnetic materials containing *f*-electrons (i.e., Ce- and Yb-containing compounds).[39−42] The onset of this behavior, T_K, decreases as a function of Co incorporation. This may be due to the increasing M1-M2 distances in the transition-metal sublattice, which would weaken the exchange interactions associated with the Kondo effect. $Ce_2Fe_{4-x}Co_xSb_{4.8}Bi_{0.2}$ (x ~ 0.5) exhibits resistivity on the order of ~98 $\mu\Omega$·cm at room temperature, which is close to an order of magnitude lower than $Ce_2Fe_4Sb_5$ (~600 $\mu\Omega$·cm at room temperature).[27] This observation is consistent with the magnetic susceptibility measurements where the ordering temperature is suppressed upon cobalt substitution. The decrease in resistivity relative to the parent compound is also consistent with the results of the $La_2Fe_{4-x}Co_xSb_{4.8}Bi_{0.2}$ (x ~ 0.5) analogue.

4. CONCLUSIONS

We have successfully grown single crystals of $La_2Fe_4Sb_5$, $La_2Fe_{4-x}Co_xSb_{4.8}Bi_{0.2}$ (x ~ 0 and 0.5), $Ce_2Fe_4Sb_5$, and $Ce_2Fe_{4-x}Co_xSb_{4.8}Bi_{0.2}$ (x ~ 0.5) for the investigation of Co incorporation in both a nonmagnetic and a magnetic rare earth analogue. The use of Bi as a low-melting flux for $La_2Fe_{4-x}Co_xSb_{4.8}Bi_{0.2}$ (x ~ 0 and 0.5) and $Ce_2Fe_{4-x}Co_xSb_{4.8}Bi_{0.2}$ (x ~ 0.5) allowed for the growth of high-quality single crystals that were suitably large enough for electrical transport and magnetic property measurements. Although Bi incorporated into the square Sb nets, it was found that the incorporation does not significantly affect the magnetic properties as compared to the $La_2Fe_4Sb_5$ and $Ce_2Fe_4Sb_5$ analogues grown in a self-flux. It is possible that single crystals of other antimonides containing square Sb nets can be grown using Bi as a flux.

The $La_2Fe_4Sb_5$ structure type is unique because of the presence of two magnetic sublattices and the triangular network of transition metal within the transition-metal−antimony sublattice. The interplay of the transition-metal and rare earth sublattices is complex with higher concentrations of Co leading to reduced magnetic frustration as evidenced by the Weiss temperature. The hysteretic behavior of $La_2Fe_{4-x}Co_xSb_{4.8}Bi_{0.2}$ (x ~ 0 and 0.5), $Ce_2Fe_4Sb_5$, and $Ce_2Fe_{4-x}Co_xSb_{4.8}Bi_{0.2}$ (x ~ 0.5) becomes more pronounced and the remanent magnetization becomes larger with the incorporation of Co. The resistivity of $Ce_2Fe_4Sb_5$ and $Ce_2Fe_{4-x}Co_xSb_{4.8}Bi_{0.2}$ (x ~ 0.5) showed that the onset of Kondo-like behavior (T_K) decreases as a function of Co concentration, indicating that the coupling of localized and conduction electrons is influenced by the distances within the transition-metal sublattice.

■ ASSOCIATED CONTENT

Ⓢ Supporting Information

The Supporting Information is available free of charge on the ACS Publications website at DOI: 10.1021/acs.inorgchem.9b00338.

Elemental analysis, Curie−Weiss fits, TGA-DSC, and crystallographic information (PDF)

Accession Codes

CCDC 1853278−1853279, 1853367, and 1895377−1895378 contain the supplementary crystallographic data for this paper. These data can be obtained free of charge via www.ccdc.cam.ac.uk/data_request/cif, or by emailing data_request@ccdc.cam.ac.uk, or by contacting The Cambridge Crystallographic Data Centre, 12 Union Road, Cambridge CB2 1EZ, UK; fax: +44 1223 336033.

■ AUTHOR INFORMATION

Corresponding Author

*E-mail: Julia.Chan@utdallas.edu.

ORCID

Ashley Weiland: 0000-0001-7198-3559
Bing Lv: 0000-0002-9491-5177
Julia Y. Chan: 0000-0003-4434-2160

Notes

The authors declare no competing financial interest.

DOI: 10.1021/acs.inorgchem.9b00338
Inorg. Chem. 2019, 58, 6028−6036

■ ACKNOWLEDGMENTS

The authors acknowledge the National Science Foundation (NSF-DMR-1700030 and NSF-DMR-1360863) for partial funding of this work. K.A.B. was supported with an American Fellowship from the American Association of University Women. This work is supported in part by the U.S. Air Force Office of Scientific Research (AFOSR) (FA9550-15-1-0236 and FA9550-19-1-0037) and by start-up funds from the University of Texas at Dallas. The authors also gratefully acknowledge support from the Office of Naval Research (N00014-15-1-2411). The authors thank Hanlin Wu for assistance with synthesis.

■ REFERENCES

(1) Wang, R.; Steinfink, H. The Crystal Chemistry of Selected AB_2 Rare Earth Compounds with Selenium, Tellurium, and Antimony. *Inorg. Chem.* **1967**, *6*, 1685−1692.

(2) Luccas, R. F.; Fente, A.; Hanko, J.; Correa-Orellana, A.; Herrera, E.; Climent-Pascual, E.; Azpeitia, J.; Pérez-Castañeda, T.; Osorio, M. R.; Salas-Colera, E.; Nemes, N. M.; Mompean, F. J.; García-Hernández, M.; Rodrigo, J. G.; Ramos, M. A.; Guillamon, I.; Vieira, S.; Suderow, H. Charge Density Wave in Layered $La_{1-x}Ce_xSb_2$. *Phys. Rev. B: Condens. Matter Mater. Phys.* **2015**, *92*, 235153.

(3) Bud'ko, S. L.; Canfield, P. C.; Mielke, C. H.; Lacerda, A. H. Anisotropic Magnetic Properties of Light Rare-Earth Diantimonides. *Phys. Rev. B: Condens. Matter Mater. Phys.* **1998**, *57*, 13624−13638.

(4) Young, D. P.; Goodrich, R. G.; DiTusa, J. F.; Guo, S.; Adams, P. W.; Chan, J. Y.; Hall, D. High Magnetic Field Sensor Using $LaSb_2$. *Appl. Phys. Lett.* **2003**, *82*, 3713−3715.

(5) Guo, S.; Young, D. P.; Adams, P. W.; Wu, X. S.; Chan, J. Y.; McCandless, G. T.; DiTusa, J. F. Dimensional Crossover in the Electrical and Magnetic Properties of the Layered $LaSb_2$ Superconductor Under Pressure. The Role of Phase Fluctuations. *Phys. Rev. B: Condens. Matter Mater. Phys.* **2011**, *83*, 174520.

(6) Sologub, O. L.; Salamakha, P. S. Rare Earth-Antimony Systems. *Handbook on the Physics and Chemistry of Rare Earths* **2003**, *33*, 35−146.

(7) Andrukhiv, L. S.; Lysenko, L. O.; Yarmolyuk, Y. P.; Hladyshevsky, E. I. Structure of the Compounds $HfCuSi_2$, $HfCuGe_2$, $ZrCuSi_2$ and $ZrCuGe_2$. *Dop. Akad. Nauk Ukrain. RSR* **1975**, *7*, 645−648.

(8) Benavides, K. A.; Oswald, I. W. H.; Chan, J. Y. Casting a Wider Net: Rational Synthesis Design of Low-Dimensional Bulk Materials. *Acc. Chem. Res.* **2018**, *51*, 12−20.

(9) Thomas, E. L.; Moldovan, M.; Young, D. P.; Chan, J. Y. Synthesis, Structure, and Magneto-Transport of $LnNi_{1-x}Sb_2$ (Ln = Y, Gd-Er). *Chem. Mater.* **2005**, *17*, 5810−5816.

(10) Liu, J. Y.; Hu, J.; Zhang, Q.; Graf, D.; Cao, H. B.; Radmanesh, S. M. A.; Adams, D. J.; Zhu, Y. L.; Cheng, G. F.; Liu, X.; Phelan, W. A.; Wei, J.; Jaime, M.; Balakirev, F.; Tennant, D. A.; DiTusa, J. F.; Chiorescu, I.; Spinu, L.; Mao, Z. Q. A Magnetic Topological Semimetal $Sr_{1-y}Mn_{1-z}Sb_2$ ($y, z < 0.1$). *Nat. Mater.* **2017**, *16*, 905−910.

(11) Kealhofer, R.; Jang, S.; Griffin, S. M.; John, C.; Benavides, K. A.; Doyle, S.; Helm, T.; Moll, P. J. W.; Neaton, J. B.; Chan, J. Y.; Denlinger, J. D.; Analytis, J. G. Observation of a Two-Dimensional Fermi Surface and Dirac Dispersion in $YbMnSb_2$. *Phys. Rev. B: Condens. Matter Mater. Phys.* **2018**, *97*, 045109.

(12) Yang, S.-Y.; Yang, H.; Derunova, E.; Parkin, S. S. P.; Yan, B.; Ali, M. N. Symmetry Demanded Topological Nodal-Line Materials. *Adv. Phys. X* **2018**, *3*, 1414631.

(13) Schoop, L. M.; Pielnhofer, F.; Lotsch, B. V. Chemical Principles of Topological Semimetals. *Chem. Mater.* **2018**, *30*, 3155−3176.

(14) Park, J.; Lee, G.; Wolff-Fabris, F.; Koh, Y. Y.; Eom, M. J.; Kim, Y. K.; Farhan, M. A.; Jo, Y. J.; Kim, C.; Shim, J. H.; Kim, J. S. Anisotropic Dirac Fermions in a Bi Square Net of $SrMnBi_2$. *Phys. Rev. Lett.* **2011**, *107*, 126402.

(15) Wang, K.; Petrovic, C. Multiband Effects and Possible Dirac States in $LaAgSb_2$. *Phys. Rev. B: Condens. Matter Mater. Phys.* **2012**, *86*, 155213.

(16) Borisenko, S.; Evtushinsky, D.; Gibson, Q.; Yaresko, A.; Kim, T.; Ali, M. N.; Buechner, B.; Hoesch, M.; Cava, R. J. Time-Reversal Symmetry Breaking Weyl State in $YbMnBi_2$. 2015, arXiv:1507.04847. *arXiv.org, e-Print arch.* https://arxiv.org/abs/1507.04847; pp 1−21.

(17) Feng, Y.; Wang, Z.; Chen, C.; Shi, Y.; Xie, Z.; Yi, H.; Liang, A.; He, S.; He, J.; Peng, Y.; Liu, X.; Liu, Y.; Zhao, L.; Liu, G.; Dong, X.; Zhang, J.; Chen, C.; Xu, Z.; Dai, X.; Fang, Z.; Zhou, X. J. Strong Anisotropy of Dirac Cones in $SrMnBi_2$ and $CaMnBi_2$ Revealed by Angle-Resolved Photoemission Spectroscopy. *Sci. Rep.* **2015**, *4*, 5385.

(18) Masuda, H.; Sakai, H.; Tokunaga, M.; Miyake, A.; Yamasaki, Y.; Shiogai, J.; Nakamura, S.; Awaji, S.; Tsukazaki, A.; Nakao, H.; Murakami, Y.; Arima, T.-H.; Tokura, Y.; Ishiwata, S. Quantum Hall Effect in a Bulk Antiferromagnet $EuMnBi_2$ with Magnetically Confined Two-Dimensional Dirac Fermions. *Sci. Adv.* **2016**, *2*, e1501117.

(19) Li, L.; Wang, K.; Graf, D.; Wang, L.; Wang, A.; Petrovic, C. Electron-Hole Asymmetry, Dirac Fermions, and Quantum Magnetoresistance in $BaMnBi_2$. *Phys. Rev. B: Condens. Matter Mater. Phys.* **2016**, *93*, 115141.

(20) Liu, J.; Hu, J.; Cao, H.; Zhu, Y.; Chuang, A.; Graf, D.; Adams, D. J.; Radmanesh, S. M. A.; Spinu, L.; Chiorescu, I.; Mao, Z. Nearly Massless Dirac Fermions Hosted by Sb Square Net in $BaMnSb_2$. *Sci. Rep.* **2016**, *6*, 30525.

(21) He, J. B.; Fu, Y.; Zhao, L. X.; Liang, H.; Chen, D.; Leng, Y. M.; Wang, X. M.; Li, J.; Zhang, S.; Xue, M. Q.; Li, C. H.; Zhang, P.; Ren, Z. A.; Chen, G. F. Quasi-Two-Dimensional Massless Dirac Fermions in $CaMnSb_2$. *Phys. Rev. B: Condens. Matter Mater. Phys.* **2017**, *95*, 045128.

(22) Klemenz, S.; Lei, S.; Schoop, L. M. Topological Semimetals in Square-Net Materials. *Annu. Rev. Mater. Res.* **2019**, DOI: 10.1146/annurev-matsci-070218-010114.

(23) Woll, P. Zur Darstellung und Strukturchemie von Erdalkali - bzw. Seltenerd-Übergangsmetall-Element-IV-bzw. Element-V-Verbindungen. Ph.D. Thesis, Technischen Hochschule Darmstadt, 1987.

(24) Doniach, S. The Kondo Lattice and Weak Antiferromagnetism. *Physica B+C* **1977**, *91*, 231−234.

(25) Stewart, G. R. Non-Fermi-Liquid Behavior in *d*- and *f*-Electron Metals. *Rev. Mod. Phys.* **2001**, *73*, 797−855.

(26) Löhneysen, H. v.; Rosch, A.; Vojta, M.; Wölfle, P. Fermi-Liquid Instabilities at Magnetic Quantum Phase Transitions. *Rev. Mod. Phys.* **2007**, *79*, 1015−1075.

(27) Phelan, W. A.; Nguyen, G. V.; Wang, J. K.; McCandless, G. T.; Morosan, E.; DiTusa, J. F.; Chan, J. Y. Discovery of Spin Glass Behavior in $Ln_2Fe_4Sb_5$ (Ln = La-Nd and Sm). *Inorg. Chem.* **2012**, *51*, 11412−11421.

(28) Watkins-Curry, P.; Pujol, K. J.; Benavides, K. A.; Burnett, J. V.; Hedlund, J. K.; Bykova, J.; McCandless, G. T.; Walker, A. V.; Chan, J. Y. Emergence of Magnetic States in $Pr_2Fe_{4-x}Co_xSb_5$ ($1 < x < 2.5$). *Inorg. Chem.* **2016**, *55*, 1946−1951.

(29) Canfield, P. C.; Kong, T.; Kaluarachchi, U. S.; Jo, N. H. Use of Frit-Disc Crucibles for Routine and Exploratory Solution Growth of Single Crystalline Samples. *Philos. Mag.* **2016**, *96*, 84−92.

(30) Krause, L.; Herbst-Irmer, R.; Sheldrick, G. M.; Stalke, D. Comparison of Silver and Molybdenum Microfocus X-ray Sources for Single-Crystal Structure Determination. *J. Appl. Crystallogr.* **2015**, *48*, 3−10.

(31) Sheldrick, G. M. SHELXT - Integrated Space-Group and Crystal-Structure Determination. *Acta Crystallogr., Sect. A: Found. Adv.* **2015**, *71*, 3−8.

(32) Sheldrick, G. M. Crystal Structure Refinement with *SHELXL*. *Acta Crystallogr., Sect. C: Struct. Chem.* **2015**, *71*, 3−8.

(33) Schwarz, U.; Tence, S.; Janson, O.; Koz, C.; Krellner, C.; Burkhardt, U.; Rosner, H.; Steglich, F.; Grin, Y. $CoBi_3$: A Binary Cobalt-Bismuth Compound and Superconductor. *Angew. Chem., Int. Ed.* **2013**, *52*, 9853−9857.

DOI: 10.1021/acs.inorgchem.9b00338
Inorg. Chem. 2019, 58, 6028−6036

(34) Tence, S.; Janson, O.; Krellner, C.; Rosner, H.; Schwarz, U.; Grin, Y.; Steglich, F. $CoBi_3$-The First Binary Compound of Cobalt with Bismuth: High-Pressure Synthesis and Superconductivity. *J. Phys.: Condens. Matter* **2014**, *26*, 395701.
(35) Walsh, J. P. S.; Clarke, S. M.; Meng, Y.; Jacobsen, S. D.; Freedman, D. E. Discovery of $FeBi_2$. *ACS Cent. Sci.* **2016**, *2*, 867−871.
(36) Schäfer, K.; Gerke, B.; Niehaus, O.; Pöttgen, R. $CeNi_{1-x}Sb_{1+y}Bi_{1-y}$ Phases with ZrCuSiAs-type and $CeNi_{1.26}Sb_2$ with $CaBe_2Ge_2$-type Structure. *Z. Naturforsch., B: J. Chem. Sci.* **2014**, *69*, 409−416.
(37) Coleman, P. Heavy Fermions: Electrons at the Edge of Magnetism. *Handbook of Magnetism and Advanced Magnetic Materials* **2007**, *1*, 95−148.
(38) Kondo, J. Resistance Minimum in Dilute Magnetic Alloys. *Prog. Theor. Phys.* **1964**, *32*, 37−69.
(39) Cox, D. L.; Zawadowski, A. Exotic Kondo Effects in Metals: Magnetic Ions in a Crystalline Electric Field and Tunneling Centers. *Adv. Phys.* **1998**, *47*, 599−942.
(40) Yang, Y.-f.; Fisk, Z.; Lee, H.-O.; Thompson, J. D.; Pines, D. Scaling the Kondo Lattice. *Nature (London, U. K.)* **2008**, *454*, 611−613.
(41) Morosan, E.; Natelson, D.; Nevidomskyy, A. H.; Si, Q. Strongly Correlated Materials. *Adv. Mater.* **2012**, *24*, 4896−4923.
(42) Canfield, P. C.; Bud'ko, S. L. Preserved Entropy and Fragile Magnetism. *Rep. Prog. Phys.* **2016**, *79*, 084506.

DOI: 10.1021/acs.inorgchem.9b00338
Inorg. Chem. 2019, 58, 6028−6036